https://doi.org/10.1016/j.fuel.2018.12.051

Soot formation and evolution characteristics in premixed methane/ethylene-oxygen-argon burner-stabilized stagnation flames

Shuyuan Liu[1, 2], Tat Leung Chan[1,2,*] , Zhu He[3], Yinyin Lu[1,2], Xiao Jiang[1,2], Fangzhou Wei[1,2]

[1]Department of Mechanical Engineering, The Hong Kong Polytechnic University, Kowloon, Hong Kong
[2]The Hong Kong Polytechnic University, Shenzhen Research Institute, Shenzhen, PR China
[3]National-provincial Joint Engineering Research Center of High Temperature Materials and Lining Technology, Wuhan, PR China

[*]Corresponding Author and E-mail: mmtlchan@polyu.edu.hk (T.L. Chan)

Abstract

The soot formation and evolution characteristics in premixed methane/ethylene-oxygen-argon flames are studied experimentally and numerically. The soot particles sampled with an in-situ probe sampling method are measured for different light hydrocarbon fuels (i.e., methane and ethylene), heights above the exit surface of the burner (HAB), equivalence ratios, ϕ and Reynolds numbers of flame jet, Re_j. A novel stochastically weighted operator splitting Monte Carlo (SWOSMC) method coupled with detailed soot model is developed to simulate the evolution of soot particle size distribution (PSD) in premixed methane/ethylene-oxygen-argon flames. The flame temperature decreases while geometric mean diameter of soot particles increases with increasing ϕ. With increasing ϕ, condensation and nucleation processes are enhanced in methane flame while coagulation and nucleation processes are enhanced in ethylene flame. Hence, these processes lead to an increase of total soot number concentration for methane flame but a decrease for ethylene flame. A distinctly different variation trend of the normalized total number density of soot particles for methane flame along with HAB can

be found for low and high studied Re_j ranges. Similarly, a distinctly different variation trend of geometric mean diameter of soot particles for ethylene flames along with HAB can also be found for low and high studied Re_j ranges. The numerical simulation results obtained via the fully validated SWOSMC method show excellent agreement with experimental results in the present study. Consistent with the experimental results, the numerical simulation results show that both condensation and nucleation rates increase and become dominant processes in the methane flame while coagulation rate increases in ethylene flame with increasing ϕ. Meanwhile, the simulated nucleation and coagulation rates along the centerline of both methane and ethylene burner flames are reversed with increasing Re_j. The present study not only verifies the competition phenomenon among different soot dynamic processes but also shows that this competition can be reversed for different Re_j ranges. These results show that the soot formation and evolution characteristics in the studied premixed methane/ethylene-oxygen-argon flames are determined by competition among different soot dynamic processes.

Keywords: Soot formation and evolution characteristics; Premixed combustion; Burner stabilized-stagnation flame; Light hydrocarbon fuels; Competition in soot dynamic processes

1. Introduction

Considerable research studies have been conducted to reveal the flow and thermal characteristics of impinging flames e.g. flame structure, flame temperature and heat transfer performance [1-9]. Due to the high convective heat transfer rate and heating temperature, impinging flame/air jets have been widely used in various practical applications including domestic heating, metallurgy and glass shaping etc. [1-6]. Chander and Ray [4] presented an

excellent review of flame impingement heat transfer. They highlighted the studies on different modes of heat transfer, flame shapes and stabilization as well as the measurement and contribution of non-luminous radiation to the overall heat transfer. Wei et al. [8, 9] investigated experimentally the heat transfer characteristics of a biogas-hydrogen flame and obtained the optimized heating distance of laminar premixed flame impinging on a flat surface. Besides abundant research studies on impingement heat transfer, there are also increasing studies on emission characteristics of impinging flames [10-14]. Combustion emissions including gaseous emissions (e.g., CO, NO_x, and HC) and particulate emission are mainly generated from fossil fuels. Recently, Wei et al. [13] investigated experimentally and numerically the emission characteristics of laminar premixed biogas-hydrogen impinging flame. Luo et al. [14] studied experimentally the effect of flame-wall interactions on the nanostructure and reactivity soot in a jet impinging ethylene diffusion flame with the special emphasis on characteristics of soot formation on the impinging plate. With growing public concern on environment, human health and global climate change, combustion pollutant emission control, particularly soot emission in impinging flames has attracted increasing attention [14-20]. Among these combustion emissions, the soot emission has been found to be responsible for several health problems including asthma, premature mortality and lung cancer etc. [14-16] as well as the climate change and global warming [14, 16].

In order to get better understanding of soot formation and evolution mechanisms derived from fuel pyrolysis or combustion under fuel rich conditions, research efforts are committed to both experimental studies and numerical simulations. Based on the concept of impinging flame, recent advances in burner-stabilized stagnation flame measurement method, probe sampling

and particle concentration and distribution measurement technology have been widely used to obtain the information of soot formation and growth in combustion flames [21-25]. The burner-stabilized stagnation flame measurement approach coupled with mobility sizing have yielded much information about the competition between different soot dynamic processes [22,24]. In order to improve the quantitative understanding of fundamental soot dynamics and overcome the probe effects in soot sampling, results of the detailed particle size distribution function (PSDF) is coupled with soot model predictions [26-30]. Saggese et al. [26] presented a detailed numerical study on the probe-induced effects on soot sampling in a burner-stabilized stagnation (BSS) ethylene and propane flames, respectively. Their research findings show that the spatial shift is weakly dependent on fuel chemistry, but is strongly dependent on burner to stagnation separation, pressure drop across the orifice, unburned gas velocity and the orifice diameter [26].

Numerical modeling and simulation methods have become a powerful computational tool in providing high resolution of time and space for soot particle size distributions. Nowadays, most of the phenomenological models of soot are based on methods for solving the population balance equation (PBE) with respect to particle number density function. Three typical numerical methods are widely used for solving PBE in terms of soot particle size distributions. These numerical methods are the sectional method [31,32], based on a direct discretization of the population balance equation [33], the Monte Carlo method [34-38] which simulates the evolution of a population of particles with stochastic methods and the moment methods [39-42] which solves the transformed moment transport equations. Among these numerical methods, Monte Carlo method is capable of obtaining highly accurate results with respect to evolution history information of soot particle size distribution [37]. Based on the direct

simulation Monte Carlo (DSMC) method [34], the authors' research group have recently developed stochastically weighted operator splitting Monte Carlo (SWOSMC) method [36-37] and differentially weighted operator splitting Monte Carlo (DWOSMC) method [38]. These modified Monte Carlo methods [36-38] exhibit high computational efficiency and accuracy in simulating complex aerosol dynamics.

Although numerous studies on soot emission characteristics have been carried out both experimentally and numerically, there are only few studies that combine experimental and numerical studies and provide a deep insight into the connection between macroscopic properties of soot particles (e.g., particle size distribution function (PSDF)) and mesoscopic soot dynamics. In fact, the interaction and competition among different soot dynamic processes (e.g., coagulation, nucleation, condensation etc.) directly affect the soot properties, which are also subject to different combustion conditions. Hence, the purpose of the present study is to provide a better insight into the interaction and competition among different soot dynamic processes and the effects on soot emission characteristics by the combined experimental and numerical approaches. In the present study, the evolution of soot PSDFs is measured using the burner-stabilized stagnation (BSS) flame and scanning mobility particle spectrometer (SMPS) technique [43]. A stochastically weighted operator splitting Monte Carlo (SWOSMC) method proposed in our previous study [36-37] is proven to have high computational efficiency and accuracy. Therefore, this newly developed SWOSMC method is further coupled with detailed and modified soot model to simulate the evolution of soot particle size distribution in premixed flames. Both premixed burner-stabilized stagnation methane/ethylene-oxygen-argon flames are measured and simulated to study the effects of fuel types, equivalence ratios and Reynolds

number of flame jet.

2. Experimental methodology

The schematic configurations of the experimental facility is shown in Fig.1. Laminar premixed flat methane (CH_4)/ethylene (C_2H_4) flame is generated by a commercial Holthuis flat flame burner (previously referred to as McKenna burner [43]) with a stainless outer layer and a 60 mm diameter stainless steel porous sintered plug cooled by cooling water. To maintain flame stabilization, the flame is isolated from surrounding ambient air by introducing a shroud of high-purity argon [43]. A 20 mm thick rectangular metal sheet is mounted above the burner as an impingement plate. The flow rates of unburned gas mixture are controlled by gas mass flow meters. The flame temperature is measured by a B-type thermocouple coated with Yttrium/ Beryllium/Oxygen (Y/Be/O) mixture to prevent surface catalytic reaction. Radiation correction for the flame temperature is made following the procedure suggested by Shaddix [44] which are well established in our Combustion and Heat Transfer Laboratory [1,2,8,9,11].

The experimental apparatus consisted of gas feeding system, the burner-stabilized stagnation flame system, gaseous and particle sampling system and the water-cooling system. A stainless steel tube with a small sampling orifice is placed across the flame to collect soot particles [43]. The position of the sampling orifice is automatically controlled by a two-dimensional traversing system. The separation distance between exit surface of the burner and the impingement plate is kept unchanged (i.e., 80 mm) in order to minimize the effect of changing sampling positions. The results show that the temperature distributions of the flame jet are only varied very slightly with different sampling heights are changed if the separation

distance is unchanged.

Fig.1. Schematic configuration of experimental apparatus.

The sampling tube is connected with two Dekati thermodiluters. Compressed air is fed into the diluters to dilute the concentration of exhaust emissions. Nitrogen is introduced and controlled to the sampling tube in order to dilute and cool down the collected soot particles containing exhaust gases instantly. The uncertainty in the flowrate is about 0.5%, mostly due to ambient temperature fluctuation. It is calculated that the dilution ratio (DR) is around 512 in the present study with relative error within 2%. Zhao et al. demonstrated [45] that the optimal dilution ratio range is 430~1000 provided that the collected soot particles could be diluted and cooled down immediately. Such similar experimental requirements and approaches of Zhao et al [45] are used in the present study. Measurement of soot particle size distribution function is carried out using TSI Scanning Mobility Particle Spectrometer (SMPS). The sampling tube is automatically moved out of the flame by a two-dimensional traversing system when a sampling collected is completed. Four sampling heights above exit surface of the burner are selected in the present study. Argon is added into the premixed fuel gases to dilute the flame and reduce the flame temperature. The details of the experimental facilities and operation parameters are summarized in Table 1.

Table 1 Details of the experimental facility and operation parameters.

The effects of fuel type, equivalence ratio, ϕ (ranging from 1.7 to 2.1), and flame ϕjet Reynolds number, Re_j (ranging from 200 to 500) on soot particle size distribution are studied.

The equivalence ratio, ϕ used is defined as follow,

$$\phi = \frac{\dot{Q}_{\text{fuel}}/\dot{Q}_{\text{ox}}}{(\dot{Q}_{\text{fuel}}/\dot{Q}_{\text{ox}})_{\text{stoich}}} \quad (1)$$

where $\dot{Q}_{\text{fuel}}$ and $\dot{Q}_{\text{ox}}$ are the volume flow rates of fuel gas (i.e., ethylene (C_2H_4) or methane (CH_4)) and oxidant, ox (i.e., oxygen (O_2)), respectively. The subscript "stoich" means the fuel and the oxidant volumetric ratio for stoichiometric combustion.

3. Numerical methodology

3.1. Gas phase model

The flame solver package OpenSMOKE [46] is used to simulate the gas phase reactions of the burner-stabilized premixed flames. This solver is an open source framework for numerical simulations of with detailed kinetic mechanisms. The species diffusion is modeled using the mixture-averaged diffusion model while thermal diffusion is considered in the species transport equations. This adopted flame solver can be easily coupled with our newly developed stochastically weighted operator splitting Monte Carlo (SWOSMC) method [36, 37]. In order to ensure the smoothness of the calculated results, the solution gradient and curvature are controlled. The detailed combustion mechanisms of methane and ethylene are based on a detailed description of the C1-C4 chemistry, which have been fully validated against the available experimental data [47]. The mechanisms also account for the formation and disappearance of soot precursors including benzene, toluene and polycyclic aromatic hydrocarbons (PAH).

As for the treatment of chemistry and flow field of gases, the detailed combustion mechanisms of methane and ethylene fuels are based on a detailed description of the C1−C4

chemistry in [32], which have been fully validated against the available experimental data [47]. The governing equations of mass, momentum and enthalpy of gas phase for the compressible laminar flow reactive flow and the conservation equation of the constituent species can be described as follows:

$$\frac{\partial \rho}{\partial t} + \frac{\partial (\rho u_j)}{\partial x_j} = S_m \tag{2}$$

$$\frac{\partial (\rho u_i)}{\partial t} + \frac{\partial}{\partial x_j}(\rho u_j u_i - \tau_{ij}) = -\frac{\partial p}{\partial x_j} + S_i \tag{3}$$

$$\frac{\partial (\rho h)}{\partial t} + \frac{\partial}{\partial x_j}(\rho h u_j - F_{h,j}) = \frac{\partial p}{\partial t} + u_j \frac{\partial p}{\partial x_j} + \tau_{ij} \frac{\partial u_i}{\partial x_j} + S_h \tag{4}$$

$$\frac{\partial (\rho Y_k)}{\partial t} + \frac{\partial}{\partial x_j}(\rho u_j Y_k + F_{k,j}) = S_k \tag{5}$$

where ρ is the mass density and t is the time where x_j denotes the Cartesian coordinate system (i= 1, 2, 3); u_j is the absolute velocity component in the x_j direction; p and τ_{ij} are the pressure and the pressure tensor component, respectively; h is the static enthalpy; $F_{h,j}$ and $F_{k,j}$ are the diffusional energy flow and diffusional flux components in the x_j direction, respectively; S_m, S_i, S_h and S_k are the source terms of mass, energy, momentum and mass production rate of kth species, respectively; Y_k is the mass fraction of the kth species.

Based on the finite volume method, the convection and diffusion terms are discretized by the second-order upwind scheme and the central difference scheme, respectively, and the coupling between velocity and pressure is completed by the pressure-implicit with splitting of operators (PISO) algorithm [13]. For the numerical calculation of the compressible reactive flow, a CHEMKIN compatible complex chemistry is incorporated in the OpenSMOKE software [46], which can solve methane and ethylene combustion reactions accordingly.

3.2.Soot model

A soot particle can be treated as a fractal-like aggregate where S, V, n_p, D_p are the surface area, volume, number of primary particles and diameter of soot aggregate, respectively, the following equations describe their relationship [48]:

$$D_p = \frac{6V}{S} \tag{6}$$

$$n_p = \frac{S^3}{36\pi V^2} \tag{7}$$

In the present study, soot dynamic processes including nucleation, surface growth, condensation, and coagulation between soot particles are included in the soot model. Nucleation of a soot particle takes place when two dimers collide to form of a spherical nucleus. The nucleation model in [35] is used in the present study, in which two naphthalene molecules form a dimer and two dimers then collide and form a spherical nucleus of diameter 0.94 nm [35]. Condensation occurs when dimers condense on soot particles. In order to keep steady state of dimers concentration, it is assumed that the formation rate of dimers is equal to the sum of nucleation and condensation rates [49]. Soot surface growth is assumed to happen through the hydrogen abstraction and C_2H_2 addition (HACA) mechanism [35,49]. Soot oxidation is not considered since oxidation is shown to have very minor effect on soot evolution in fuel-rich premixed flames [50-52].

A well-known simplified soot inception model in [35] is used to calculate the soot nucleation rate. In this model, the soot inception is correlated with acetylene concentration and takes the form as,

$$J_0(t) = C_n N_A \left(\rho \frac{Y_{\text{actylene}}}{W_{\text{actylene}}}\right) \exp\left(-\frac{21{,}000}{T}\right) \tag{8}$$

where ΔG^* is the free energy that is required to form a stable nucleus and C_n is a constant, $54 s^{-1}$, N_A is Avagadro number, ρ is the mixture denstiy, T is the temperature, Y_{actylene} and

W_{actylene} are the mass fraction and molecular weight of acetylene, respectively.

The surface growth term is modified based on the model in [35],

$$G_{s,i} = k_s C_g \alpha \chi_s \, m_i \Delta_s S_i N_i \tag{9}$$

where $G_{s,i}$ is the surface growth rate of the i-th particle due to the surface chemical reactions of soot aggregates, k_s is the per-site rate coefficient, C_g is the concentration of gaseous species, α is the fraction of reaction sites available, χ_s is the number density of active surface sites, Δ_s is the mass change due to the surface growth, and m_i, S_i, N_i are the mass, surface area and number density of the i-th particle, respectively.

Compared with the above deterministic processes, coagulation is a stochastic process referring to the formation of a larger particle or aggregate due to collision of two smaller particles. The collision diameter of soot aggregate, D_c can be calculated from soot volume, surface area and soot fractal dimension as,

$$D_c = 6(36\pi)^{-1/D_f} V^{1-2/D_f} S^{3/D_f - 1} \tag{10}$$

where $D_f = 1.8$ is the fractal dimension of soot aggregate, and V and S are soot particle volume and surface area, respectively. For the transition flow regime in the present study, the harmonic mean of the continuum and free molecular coagulation kernels [53] is used as,

$$\frac{1}{\beta_t(n_i,n_j)} = \frac{1}{\beta_c(n_i,n_j)} + \frac{1}{\beta_f(n_i,n_j)} \tag{11}$$

where $\beta_t(n_i,n_j)$ is the coagulation kernel in the transition regime.

For free molecular regime, the coagulation kernel $K(u,v)$ can be written as follows [36],

$$\beta_f(u,v) = B_f\left(u^{\frac{1}{3}} + v^{\frac{1}{3}}\right)^2 \left(\frac{1}{u} + \frac{1}{v}\right)^{1/2} \tag{12}$$

where B_f is a collision parameter dependent on temperature, u and v are the volume of the spherical colliders, respectively.

In a continuum regime, the coagulation kernel for spherical particles of size u and v can be written as follows [36]:

$$\beta_c(u,v)=B_c[2+(\frac{u}{v})^{\frac{1}{3}}+(\frac{v}{u})^{\frac{1}{3}}] \tag{13}$$

where B_c is a collision parameter dependent on temperature; u and v are the volume of the spherical colliders, respectively.

The evolution of soot particle number density, $n(t,x;\varphi)$ is described by PBE as follows,

$$\frac{\partial n(t,\vec{x};\varphi)}{\partial t}+\frac{\partial un(t,\vec{x};\varphi)}{\partial x_j}=\dot{n}(t,\vec{x};\varphi) \tag{14}$$

where $\dot{n}(t,\vec{x};\varphi)$ is a source term accounting for the physical and chemical processes that may affect soot particle number density, φ is a vector of internal coordinates of soot particles, which include particle volume and surface area in the present study, $\vec{x}$ is a vector for the position of soot particle. Diffusive term is not considered in Equation (6) because of the high Schmidt number of soot particles [54]. In addition, thermophoresis effect is also neglected since it is shown to have very minor effect on transport of soot particles in premixed flames [55-57].

The source term $\dot{n}(t,\vec{x};\varphi)$ is defined as,

$$\dot{n}(t,\vec{x};\varphi)=[\dot{n}(t,\vec{x})]_{\text{nuc}}+[\dot{n}(t,\vec{x};\varphi)]_{\text{coag}}+[\dot{n}(t,\vec{x};\varphi)]_{\text{cond}}+[\dot{n}(t,\vec{x};\varphi)]_{\text{surf}} \tag{15}$$

where the terms on the right hand side of Equation (15) represent the nucleation, coagulation, condensation and surface growth processes of soot particles, respectively.

3.3. Monte Carlo method

In the present study, a newly developed stochastically weighted operator splitting Monte

Carlo (SWOSMC) method in our previous research works [36, 37] is further modified and implemented to simulate the evolution and formation of soot particles. Specifically, all the soot dynamic processes are divided into two categories: stochastic process (i.e., coagulation) and deterministic processes (i.e., nucleation, surface growth, and condensation). In order to handle the significantly different characteristic time scales between stochastic collision process and other processes (i.e., nucleation, surface growth, and condensation), a second order Strang splitting scheme [35, 36] is implemented. With this operator splitting approach, the matrix of collision kernel, β_{ij} is updated only once every time step, Δt so that the computational cost is greatly reduced [35-37]. The deterministic processes are simulated via integration using a self-adaptive fifth-order Runge-Kutta method [36] over the calculated time step. The stochastic process (i.e., coagulation) is simulated using the SWOSMC method [36].

The SWOSMC method in the present study considers a set of N_i notional particles in a reactor cell of volume, Ω_i, where i is the index of the discrete time, t_i. A notional particle is associated with a varying mass weight, $w_i(t)$ of real soot particle of volume, $V_i(t)$ and surface area, $S_i(t)$. The main idea of the present method is to introduce stochastic weights to various notional particles according to the mass change caused by different soot dynamic processes so as to improve the numerical stability of the Monte Carlo method. The advantage of the SWOSMC method lies in that when mass weights are adhered to numerical particles. In other words, numerical particles are connected with a certain mass of real soot particles. Therefore, the total number of notional particles remains constant and no re-sampling is needed for coagulation process [36-37, 58].

For computation of coagulation, the collision criterion in [36] should be reached. The

volume of the i-th notional particle after an integration time step becomes the total volume of the i-th notional particle and its collision partner, while the weight of i-th numerical particle remains unchanged as the volume is conserved. In order to reduce stochastic error of Monte Carlo simulation results, each simulation run is repeated 128 times and the final simulation results are the average of all the repeated simulation results [35-36].

The surface area of the newly formed larger aggregate is a function of both aggregate mass and number of primary particles, and is computed with the method according to [59]. For integration of nucleation, only a certain mass of new particles with the minimum nucleus of diameter 0.94 nm [35] is created and added to the notional particle system. Condensation and surface growth are also integrated with a self-adaptive fifth-order Runge-Kutta method in [36].

By introducing of the variable mass weights to numerical particles, the weights $w_i(t)$ evolve with time for the mass-varying process such as condensation and evaporation. In here, nucleation is conducted by creating a certain mass of new particles according to the nucleation rate which is independent of pre-existing particles. The main algorithm of the newly developed SWOSMC method over a time period [0, T] is presented [36] as follows:

(1) Initialization: Set the initial size and weight for soot particles, [(yi_0, wi_0), i =1, 2, ..., N_0];

(2) Operator splitting over time loop [0, T]: Integration of the population balance equation (i.e., Eqs. (6) and (7)) from t_k to t_{k+1}, where $t_{k+1}= t_k+\tau_k$, and τ_k is the integration time step;

   (a) Integration of coagulation based on the above weighted Monte Carlo methods;

   (b) Integration ordinary differential equation (ODE) that governs condensation using fourth order Runge-Kutta method; and

   (c) Integration of nucleation: creation of new particles, J.

(3) Updating the particle system and return particle variables to the flow field computation; and

(4) When $t = T_{stop}$, the numerical simulation is stopped and an average of the results is taken.

4. Results and discussion

4.1 Validation of the modified SWOSMC method

In the present study, our developed and modified SWOSMC method is first validated by comparing with available experimental results [60] and numerical simulation results by direct simulation Monte Carlo (DSMC) method [35]. The similar experimental setup in [60] is also used in the present study. The ethylene–oxygen flame is generated by a water-cooled porous burner, b plug with diameter, d_b and temperature, T_b [35,60]. A circular aluminum plate positioned above a specified separation distance from the burner is used as a stagnation plate with surface temperature, T_s. The equivalence ratio of unburned gas used is 2.07 [60]. The dependence of soot formation and evolution characteristics on d_b, T_b and T_s is weak according to the findings in [35,60]. The total number concentration, volume fraction and mobility diameter of soot particles are measured. Boundary conditions are set at the exit surface of the burner (T_b = 473 K) and at the impingement plate (T_s = 500 K). The impingement plate is treated as a non-slip wall. Composition and mass flow rate of the cold gas mixture (i.e. fuel gas, oxygen and argon) are specified at the exit surface of burner. The ethylene combustion mechanism including 158 species and 1804 reactions in [61] is used in this numerical simulation.

Fig. 2 shows the number density and volume fraction of soot particles obtained from numerical simulation and experimental results of premixed ethylene flames in [60]. Apart from

the results of small height above the burner (HAB) i.e. near the exit surface of the burner, the numerical simulation results obtained from this modified SWOSMC method shows excellent agreement with both the experimental results in [60] and the numerical simulation results by DSMC in [35]. The discrepancy near the exit surface of the burner may be due to the cooling effect of unburned cold gas mixture. This discrepancy was also identified in [35]. With the increase of HAB, both number density and volume fraction of soot particles obtained from this modified SWOSMC agree well with the experimental results. In addition, the numerical simulation results obtained with the modified SWOSMC shows better agreement with experimental results in [30] than those results obtained via DSMC in [35]. These results also further validate the reliability and capability of this modified SWOSMC method in simulating soot formation and evolution in premixed ~~impinging~~ flames in the present study.

Fig. 2. A modified SWOSMC model validation with experimental results [60] and DSMC results [35]: (a) soot number density and (b) soot volume fraction for different HAB.

4.2 Effect of equivalent ratio on soot formation and evolution characteristics

The flame temperatures of methane and ethylene for different equivalence ratios, ϕ at Reynolds number of jet flame, Re_j = 600 are shown in Figs. 3 and 4, respectively. The flame temperatures are measured at different HAB along the centerline ranging from 2 cm to 6 cm for both methane and ethylene flames, respectively. It can be seen that the flame temperature of both methane and ethylene flames increase with the increase of HAB for a given equivalence ratio, ϕ. This is because the higher heat of combustion is generated as more fuel is consumed with the development of jet flame. With the equivalence ratio increasing from 1.7 to 2.1 in the present study, the flame temperature of both methane and ethylene flames decrease because of

the extra fuel supply in these fuel-rich combustion. A comparison between flame temperature of methane and ethylene shows that ethylene has a relatively higher flame temperature if the equivalence ratio and Reynolds number of jet flame are the same. However, the variation of flame temperature of ethylene is smaller than that methane when equivalence ratio, ϕ is larger than 1.7 which may be due to the different fuel types.

Fig. 3. Flame temperatures of methane at Re_j=600 for different ϕ and HAB.

Fig. 4. Flame temperatures of ethylene at Re_j=600 for different ϕ and HAB.

Soot particle size distribution (PSD) of premixed methane and ethylene flames for different equivalence ratios, ϕ as shown in Figs. 5 and 6. For a small sampling heights (i.e., HAB = 3cm), significantly varying PSDs of soot particles can be observed for both methane and ethylene flames with ϕ increasing from 1.7 to 2.1 as shown in Figs. 5(a) and 6(a). Fig. 5(a) shows that the PSD becomes wider with the increase of equivalence ratio, which is the consistent with the increasing total soot particle number concentration as shown in Fig. 7(a). In Fig. 7, the total soot number concentration (#/cm^3) of methane flame is normalized with 1.0×10^8(#/cm^3) because the order of magnitude of total soot number concentration in Fig. 7 is 10^8. Similarly, the total soot number concentration (#/cm^3) of ethylene flame is normalized with 1.0×10^7(#/cm^3) because the order of magnitude of total soot number concentration in Fig. 8 is 10^8. Fig. 7(b) shows the geometric mean diameter of soot particles in the methane flame increases from 30.0 nm to 47.8 nm with increasing ϕ from 1.7 to 1.8 and then gradually increases to 66.1 nm at ϕ = 2.1. Fig. 7(b) also shows a stable stage of geometric mean diameter with increasing ϕ from 1.8 to 2.0 although the total soot particle number concentration increases

in this range of ϕ. The results in Fig. 5(a) and Fig. 7 imply that competition exists between nucleation and other processes (e.g., coagulation and surface growth processes). This similar competition phenomenon between nucleation and coagulation processes has also been found in many research studies including turbulent particulate flows [37], soot dynamics in both premixed flames [22,24] and non-premixed flames [35]. Although nucleation process is enhanced with increasing ϕ to generate an increasing number of soot nucleus with the smallest size, the soot particles are also enlarged by coagulation and surface growth processes to yield a generally increasing geometric mean diameter of soot particles as shown in Fig. 7(b). Fig. 6(a) shows the PSD of soot particles in ethylene flame becomes wider and moves towards the upper end of the particle size range. Meanwhile, Fig. 8(a) shows that the normalized total number concentration of soot particles in ethylene flame decreases significantly. Fig. 8(b) shows the geometric mean diameter increases from 50 nm to 103 nm. These results could be attributed to the domination of agglomeration and coagulation in the flame. The combustion temperatures of ethylene in the present experiments basically higher than 1400 K. The pyrolysis and more frequent collisions are expected to take place in ethylene flame which enhances the coagulation and agglomeration processes, and increases geometric mean diameter of soot particles. On the other hand, the higher carbon content of ethylene molecule than methane molecule leads to a higher content of hydrocarbons (HC) in ethylene flame, thus producing a larger portion of PAH molecules [35,60]. This means higher the chance for soot particles or precursors to collide with others. Therefore, the total soot particle number concentration decreases while the geometric mean diameter increases with the increasing equivalence ratio. As shown in Fig. 6, there is relatively more significant deviation between experiment and

simulation results at ϕ=1.7, in which the simulation results are lower than that of experiments, particularly in Fig. 6(b), i.e. HAB=4cm. However, when referred to Fig. 8(a), it can be observed that the normalized total particle number concentration at HAB=4cm is the largest when compared with those at the other heights (HAB= 3, 5 and 6 cm). When referred to Fig. 8(b), it can observed that the geometric mean diameter of soot particles at HAB = 4 cm is the smallest when compared with those at the other heights (HAB = 3, 5 and 6cm). Hence, these obtained results imply that the soot nucleation process is the dominant process at ϕ = 1.7, when HAB = 4 cm. Therefore, the deviation between experimental and numerical simulation result at ϕ = 1.7 is mostly likely to be caused by the underestimated nucleation rate. The nucleation model adopted from Lucchesi et al. [35] is used in the present study, which is based on the assumption that nucleation rate is mainly determined by two classes of collision, i.e., collision between naphthalene molecules to form dimers and then collision between dimers to form spherical nucleus. This assumption renders very accurate nucleation model when the equivalence ratio is intermediate or high (i.e., the concentrations of naphthalene and dimers are high) but less accurate when the equivalence ratio is small [35].

Fig. 5. Soot size distribution of methane flame at Re_j = 600 for different ϕ and HAB.

Fig. 6. Soot size distribution of ethylene flame at Re_j = 600 for different ϕ and HAB.

Fig. 7. Normalized total number concentration, N_t and geometric mean diameter of soot particles of methane flame at Re_j = 600 for different ϕ and HAB.

Fig. 8. Normalized total number concentration, N_t and geometric mean diameter of soot particles of ethylene flame at Re_j = 600 for different ϕ and HAB.

The evolution of soot particles in both methane and ethylene flames can be obtained by observing the PSDs sampled at different HAB along the centerline of the flame. For soot particles generated in methane flame, Figs. 5 and 7 show that with increasing HAB = 3 to 4 cm, both the normalized total particle number concentration and the geometric mean diameter of soot particles increase for almost all the studied equivalence ratios. A crossing is observed for geometric mean diameters at HAB = 3 and 4 cm when $\phi = 2.1$. However, when HAB reaches 5 cm or above, the normalized total number concentration and geometric mean diameter of soot particles in methane flames no longer increase monotonously with the equivalence ratio as shown in Figs. 5 and 7. Fig. 7 shows that the normalized total soot number concentration and the geometric mean diameter of soot particles both decrease after $\phi = 2.0$ at HAB = 5 cm or above. These findings show that coagulation becomes the dominant soot dynamic process for highly fuel-rich methane flame (i.e., $\phi = 2.0$ or above) sampled at higher position (HAB = 5cm or above).

Similar results can be observed for ethylene flame as shown in Figs. 6 and 8. Fig. 6 shows that the PSD of soot particles in ethylene flame becomes wider and moves towards the upper end of the particle size range. Fig. 8(a) shows that for all studied equivalence ratios, the normalized total number concentration of soot particles increases when HAB increases from 3 to 4 cm, but decreases when HAB further increases from 4 to 6 cm. This is because the temperature of ethylene flame in Fig. 4 increases with HAB. The increasing temperature promotes the combustion and pyrolysis reactions of ethylene, which in turn increases the nucleation rate of soot precursors. Therefore, the normalized total soot particle number concentration in Fig 8(a) increases significantly with HAB increasing from 3 to 4 cm. However,

with further increasing in HAB from 4 to 6 cm, the increasing soot particle number concentration enhances the coagulation and agglomeration processes, which decreases the normalized total soot number concentration and increases the geometric mean diameter of soot particles as shown in Fig. 8(b). In addition, the weakening of the shielding protection of argon gas with increasing HAB causes the surrounding air entrainment in the near-impingement plate flame region. So the soot particle number concentration further decreases due to extra dilution effect by air entrainment. The comparison of soot formation and evolution characteristics in methane and ethylene flames in the present study shows that nucleation is dominant in methane flame while coagulation is dominant in the ethylene flame due to their different nucleation rates of precursors. According to Glassman and Yetter [62], the root of the soot formation process is the polymerization of –C=C−, which can be very easily initiated in ethylene flame. The increase of temperature has detrimental effect in the formation of large soot particles. On the other hand in methane flame, the polymerization process of –C=C– bonds is not initially available and the increase in temperature facilitates the pyrolysis of the fuel that is necessary in order for their formation to get initiated. As a result, the increase of temperature would facilitates the soot formation. The variation of –C=C– bonds in methane and ethylene flames is closely related to the soot dynamic processes which determines the characteristics of soot formation and evolution characteristics. In fact, the experimental and numerical simulation results in the present study are consistent with the analysis of Glassman and Yetter based on the variation of –C=C– bonds [62]. The present study provides another perspective on the characteristics of soot formation and evolution in premixed flames.

4.3 Effect on Reynolds number of flame jet on soot formation and evolution characteristics

The effect of Re_j on the flame temperature of methane and ethylene fuels are shown in Figs. 9 and 10, respectively. Since fuel gases (i.e. methane and ethylene) increase proportionally with oxygen, the heat of combustion increases accordingly with increasing Re_j. Therefore, flame temperatures increase significantly with Re_j for both methane and ethylene fuels. With the increasing of HAB along the centerline of the flame jet, flame temperature also increases slightly when Re_j is kept constant due to flame diffusion.

Fig. 9. Flame temperature of methane at $\phi = 2.0$ for different Re_j and HAB.

Fig. 10. Flame temperature of ethylene at $\phi = 2.0$ for different Re_j and HAB.

With increasing Re_j from 300 to 700, the PSD of soot particles in methane flames becomes narrower and higher for all studied HABs as shown in Fig. 11. Meanwhile, the effect of sampling height, HAB on PSD of soot particles in methane flame is very slight. Fig. 13 shows that both the normalized total number concentration and geometric mean diameter of soot particles decreases with increasing Re_j from 300 to 700. This may be attributed to the shortening residence time of soot precursors in the flame with increasing Re_j (i.e., increasing jet velocity), which decreases the number of soot precursors as well as the coagulation events between soot particles. It is worth to note that at lower Re_j (i.e., below 500), the normalized total number concentration of soot particles in Fig. 13(a) first increases and then decreases with increasing HAB from 2 to 6cm. Meanwhile, a distinctly different variation trend of the normalized total number concentration of soot particles along with increasing HAB can be observed at relatively higher Re_j (i.e., above 500). This might be because soot dynamics is firstly dominated by nucleation and then by coagulation at low Re_j. However, the competition

between nucleation and coagulation is reversed at relatively high Re_j where soot dynamics is firstly dominated by coagulation and then by nucleation when Re_j is relatively high. This can be explained by the enhanced mixing and collisions among soot particles with the increase of Re_j. This finding is also consistent with our previous study [37] that increasing Re_j will enhance mixing and collision frequency among particles if the residence time of particles is at proper range. Fig. 13(b) shows the net effect of competition between nucleation and coagulation is to generate larger soot particles with increasing HAB.

Fig. 12 shows that the effect of Re_j on PSD of soot particles in ethylene flame is quite minor at lower sampling positions (i.e., HAB = 2 and 4cm). However, significant variations of PSD are observed with increasing Re_j from 300 to 700 at HAB = 6cm. Fig. 14(a) shows that the normalized total number concentration of soot particles varies significantly with Re_j at HAB = 2 and 6 cm while varies very slightly at HAB = 4cm. The variation trend in Fig. 14(a) implies that the competition among nucleation, condensation, surface growth and coagulation is quite different at different HABs. Fig. 14(b) shows similar variation trend to that in Fig. 13(a). With increasing HAB from 2 to 6 cm, the geometric mean diameter increases when Re_j is lower than 500 but decreases when Re_j is higher than 500 as shown in Fig. 14(b). These results imply that coagulation is dominant for lower Re_j (i.e., below 500) while nucleation is dominant for higher Re_j (i.e., above 500) for ethylene flame. This might be due to the relatively higher soot volume concentration in ethylene flame, which leads to high coagulation rates even for low Re_j. With Re_j exceeding 500, the decreasing residence time and delayed mixing of soot precursors weakens coagulation process. Therefore, nucleation process becomes dominant as the total volume flow rate of fuel gas increases with increasing Re_j. These findings are also consistent

with many similar research studies on competition among different particle dynamic processes [22,24,35,37]. Particularly, the effect of Re_j on particle mixing and competition among simultaneous aerosol dynamic processes has been studied and verified in our previous study [37]. The different variation trends of soot particles with Re_j and HAB also reflect the different sooting tendency of methane and ethylene flames as shown in Figs. 13 and 14, respectively.

Fig. 11. Soot size distribution of methane flame at $\phi = 2.0$ for different Re_j and HAB.

Fig. 12. Soot size distribution of ethylene flame at $\phi = 2.0$ for different Re_j and HAB.

Fig. 13. Normalized total number concentration, N_t and geometric mean diameter of soot particles of methane flame at at $\phi = 2.0$ for different Re_j and HAB.

Fig. 14. Normalized total number concentration, N_t and geometric mean diameter of soot particles of ethylene flame at at $\phi = 2.0$ for, Re_j and HAB.

5. Conclusions and outlook on future research work

Soot formation and evolution characteristics in premixed methane/ethylene-oxygen-argon flames for different equivalence ratios, ϕ and Reynolds numbers of the flame jet, Re_j are studied experimentally and numerically. A modified SWOSMC method coupled with detailed combustion and soot model is developed. The main conclusions are as follows:

1. Excellent agreement between the numerical simulation results obtained between the developed SWOSMC method and available experimental results as well as DSMC method is obtained and validated. Furthermore, the modified SWOSMC method achieves better agreement than DSMC method when compared with the available experimental results. The developed SWOSMC method is proven to be capable of predicting soot particle size distribution with excellent computational accuracy and efficiency.

2. The flame temperature is higher at lower ϕ while geometric mean diameter of soot particles increases with increasing ϕ. With the increase of ϕ, condensation and nucleation processes are enhanced in methane flame while coagulation and nucleation processes are enhanced in ethylene flame. Hence, these processes lead to an increase of total soot particle number concentration for methane flame but a decrease for ethylene flame.
3. The present study not only verifies the competition phenomenon among different soot dynamic processes but also shows that this competition can be reversed for different Re_j ranges. A distinctly different variation trend of the normalized total number concentration of soot particles for methane flame along with HAB can be found for low and high studied Re_j ranges. Similarly, a distinctly different variation trend of geometric mean diameter of soot particles for ethylene flame along with HAB can be found for low and high studied Re_j ranges. These findings show that the competition among different soot dynamic processes determines the soot size distribution and evolution.
4. The present combined experimental and numerical studies provide a better insight into the connection between macroscopic properties of soot particles (e.g. PSDF) and micro- or meso-scopic soot dynamic processes. It is found that the competition among soot dynamics can be reversed by varying operation parameters, which is of significance in soot emission control.
5. Recommendations for future research work in the present study are focused mainly on two aspects. Firstly, the development of integrated soot formation and evolution model is recommended to provide better prediction of soot emission characteristics in wide operation conditions. Secondly, the combined experimental and numerical studies on

interaction between gaseous and particulate emissions are also recommended.

Acknowledgements

This work was supported by the financial support from the National Natural Science Foundation of China (Project No. 11572274), and the Central Research Grant (Project No. 4-BCD3) and Mechanical Engineering Department (Project No. 88Y9) of The Hong Kong Polytechnic University.

References

[1] L.L. Dong, C.S. Cheung, C.W. Leung, Heat transfer characteristics of an impinging butane/air flame jet of low Reynolds number, Exp. Heat Transfer 14(2001) 265-282.
[2] T.L. Chan, C.W. Leung, K. Jambunathan, S. Ashforth-Frost, Y. Zhou, M.H. Liu, Heat transfer characteristics of a slot jet impinging on a semi-circular convex surface. Int. J. Heat Mass Tran. 45(2002) 993-1006.
[3] W. Zhang, J. Wang, Q. Yu, J. Wu, Z, Meng, Z.H. Huang, Investigation of the fuel effects on burning velocity and flame structure of turbulent premixed flames based on leading points concept, Combust. Sci. Technol. 11(2018) 1-23.
[4] S. Chander, A. Ray, Flame impingement heat transfer: A review, Energ. Convers. Manage. 46(2005) 2803-2837.
[5] S. Guo, J. Wang, X. Wei, S. Yu, M. Zhang, Z.H. Huang, Numerical simulation of premixed combustion using the modified dynamic thickened flame model coupled with multi-step reaction mechanism, Fuel 233 (2018) 346–353.
[6] P. Singh, S. Chander, Heat transfer and fluid flow characteristics of a pair of interacting dual swirling flame jets impinging on a flat surface, Int. J. Heat Mass Tran. 124(2018) 90-108.
[7] C. Saha, R. Ganuly, A. Datta, Heat transfer and emission characteristics of impinging rich methane and ethylene jet flame, Exp. Heat Transfer 21(2008) 169-187.
[8] Z.L. Wei, H.S. Zhen, C.W. Leung, C.S. Cheung, Z.H. Huang, Heat transfer characteristics and the optimized heating distance of laminar premixed biogas-hydrogen Bunsen flame impinging on a flat surface, Int. J. Hydrogen Energ. 40(2015) 15723-15731.
[9] Z.L. Wei, C.W. Leung, C.S. Cheung, Z.H. Huang, Effects of H_2 and CO_2 addition on the heat transfer characteristics of laminar premixed biogas-hydrogen Bunsen flame, Int. J. Heat Mass Tran. 98(2016) 359-366.
[10] D.P. Mishra, Emission studies of impinging premixed flames, Fuel 83(2004) 1743-1748.
[11] H.B. Li, H.S. Zhen, C.W. Leung, C.S. Cheung, Effects of plate temperature on heat transfer and emissions of impinging flames, Int. J. Heat Mass Transfer 53(2010) 4176-4184.

[12] Z. Si, N. Shimasaki, K. Nishida, Y. Ogata, M. Guo, C.L. Tang, Z.H. Huang, Experimental study on impingement spray and near-field spray characteristics under high-pressure cross-flow conditions, Fuel 218(2018) 12-22.

[13] Z.L. Wei, H.S. Zhen, C.W. Leung, C.S. Cheung, Z.H. Huang, Experimental and numerical study on the emission characteristics of laminar premixed biogas-hydrogen impinging flame, Fuel 195(2017) 1-11.

[14] M. Luo, Y. Ying, D. Liu, Soot in flame-wall interactions: views from nanostructure and reactivity, Fuel, 212(2018), 117-131.

[15] H. Wang, Formation of nascent soot and other condensed-phased materials in flames. Proc. Combust. Inst. 33(2011) 41-67.

[16] M.O. Andreae, The dark side of aerosols, Nature 409(2001) 671-672.

[17] E. Tomita, Y. Hamamoto, H. Tsutsumi, T. Watanabe, S. Yoshiyama, Visualization of ambient air motion and entrainment into a transient gas jet impinging on a flat wall, SAE Technical Paper, 952513; 1995.

[18] X.G. Wang, Z.H. Huang, W. Zhang, O.A. Kuti, K. Nishida, Effects of ultra-high injection pressure and micro-hole nozzle on flame structure and soot formation of impinging diesel spray, Appl. Energ. 88(2011) 1620-1628.

[19] L.M. Pickett, J.L. Javier, Jet-wall interaction effects on diesel combustion and soot formation, SAE Technical Paper, 2005-01-0921, 2005.

[20] D.R. Tree, K.I. Svensson, Soot processes in compression ignition engines, Prog. Energ. Combust. 33(2007) 272-309.

[21] A.D. Abid, N. Heinz, E.D. Tolmachoff, D.J. Phares, C.S. Campbell, H. Wang, On evolution of particle size distribution functions of incipient soot in premixed ethylene–oxygen–argon flames, Combust. Flame 154(2008) 775-788.

[22] A.D. Abid, J. Camacho, D.A. Sheen, H. Wang, Quantitative measurement of soot particle size distribution in premixed flames-The burner-stabilized stagnation flame approach, Combust. Flame 156(2009) 1862-1870.

[23] C. Song, L. Hong, X. Wang, Z. Li, N. Chen, Z. Zhang, Effect of temperature on soot nanostructure and morphology in CH_4-O_2 premixed flames, J. Combust. Sci. Technol. 19(2013) 115-120.

[24] J. Camacho, A.V. Singh, W. Wang, R. Shan, E.K.Y. Yapp, D. Chen, M. Kraft, H. Wang, Soot particle size distributions in premixed stretch-stabilized flat ethylene–oxygen–argon flames. Proceedings of the Combustion Institute, 36 (2017) 1001-1009.

[25] B. Lin, H. Gu, H. Ni, B. Guan, Z. Li, D. Han, C. Gu, C. Shao, Z. Huang, H. Lin, Effect of mixing methane, ethane, propane and ethylene on the soot particle size distribution in a premixed propene flame, Combust. Flame 193(2018) 54-60.

[26] C. Saggese, A. Cuoci, A. Frassoldati, A., S. Ferrario, J. Camacho, H. Wang, T. Faravelli, Probe effects in soot sampling from a burner-stabilized stagnation flame, Combust. Flame 167 (2016) 184-197.

[27] G. Chen, L. He, J. Camacho, B. Lin, C. Shao, R. Li, H. Gu, B. Guan, Z. Huang, H. Wang, Particle size distribution of nascent soot in lightly and heavily sooting premixed ethylene flames. Combust. Flame 165 (2016) 177-187.

[28] R.P. Lindstedt, B.B.O. Waldheim, Modeling of soot particle size distributions in premixed

stagnation flow flames, Proc. Combust. Inst. 34 (2013) 1861-1868.
[29] J. Camacho, S. Lieb, H. Wang, Evolution of size distribution of nascent soot in n- and i-butanol flames, Proc. Combust. Inst. 34 (2013) 1853-1860.

[30] E. Yapp, D. Chen, J. Akroyd, S. Mosbach, M. Kraft, H. Wang, Numerical simulation and parametric sensitivity study of particle size distributions in a BSS flame, Combust. Flame 162 (2015) 2569-2581.
[31] F. Gelbard, Y. Tambour, J.H. Seinfeld, Sectional representations for simulating aerosol dynamics, J. Colloid Interf. Sci. 76 (1980) 541-556.
[32] C. Saggese, S. Ferrario, J. Camacho, A. Cuoci, A. Frassoldati, E. Ranzi, H. Wang, T. Faravelli, Kinetic modeling of particle size distribution of soot in a premixed burner-stabilized stagnation ethylene flame, Combust. Flame 162 (2015) 3356-3369.
[33] D. Ramkrishna, Population balances: theory and applications to particulate systems in engineering, Academic press, Cambridge (Massachussets, US), 2000.
[34] G. Bird , Direct simulation and the boltzmann equation, Phys. Fluids 13 (1970) 2676-2681.
[35] M. Lucchesi, A. Abdelgadir, A. Attili, F. Bisetti, Simulation and analysis of the soot particle size distribution in a turbulent nonpremixed flame, Combust. Flame 178 (2017) 35-45.
[36] S. Liu, T.L. Chan, A stochastically weighted operator splitting Monte Carlo (SWOSMC) method for the numerical simulation of complex aerosol dynamic processes, Int. J. Numer. Methods Heat Fluid Flow 27 (2017) 263-278.
[37] S. Liu, T.L. Chan, A coupled CFD-Monte Carlo method for simulating complex aerosol dynamics in turbulent flows. Aerosol Science and Technology, 51(2017) 269-281.
[38] H.M. Liu, T.L. Chan, A differentially weighted operator splitting Monte Carlo method for simulating complex aerosol dynamic processes, Particuology, 36 (2018) 114-126.
[39] M. Frenklach, S.J. Harris, Aerosol dynamics modeling using the method of moments, Journal of Colloid & Interface Science, 118 (1987) 252-261.
[40] M. Yu, J. Lin, T.L. Chan, A new moment method for solving the coagulation equation for particles in Brownian motion, Aerosol Sci. Technol. 42 (2008) 705-713.
[41] S. Salenbauch, A. Cuoci, A. Frassoldati, C. Saggese, T. Faravelli, C. Hasse, Modeling soot formation in premixed flames using an extended conditional quadrature method of moments, Combust. Flame 162(2015) 2529-2543.
[42] T.L. Chan, S.Y. Liu, Y. Yue, Nanoparticle formation and growth in turbulent flows using the bimodal TEMOM, Powder Technology, 323 (2018) 507-517.
[43] S. Li, Y. Ren, P. Biswas, S.D. Tse, Flame aerosol synthesis of nanostructured materials and functional devices: processing, modeling, and diagnostics, Progress in Energy & Combustion Science, 55 (2016) 1-59.
[44] C.R. Shaddix, Correcting thermocouple measurements for radiation loss: a critical review, Proc. 33rd Natl. Heat Transf. Conf., Albuquerque, NM, 1999, pp. 1-10.
[45] B. Zhao, Z. Yang, Z. Li, M.V. Johnston, H. Wang, Particle size distribution function of incipient soot in laminar premixed ethylene flames: effect of flame temperature. Proceedings of the Combustion Institute, 30(2005) 1441-1448.
[46] A. Cuoci, A. Frassoldati, T. Faravelli, E. Ranzi, Opensmoke++: an object-oriented framework for the numerical modeling of reactive systems with detailed kinetic

mechanisms. Computer Physics Communications, 192(2015) 237-264.
[47] E. Ranzi, A. Frassoldati, R. Grana, A. Cuoci, T. Faravelli, A. Kelley, C. Law, Hierarchical and comparative kinetic modeling of laminar flame speeds of hydrocarbon and oxygenated fuels, Prog. Energy Combust. Sci. 38 (2012) 468-501.
[48] S. Park , S. Rogak , A one-dimensional model for coagulation, sintering, and surface growth of aerosol agglomerates, Aerosol Sci. Technol. 37 (2003) 947-960.
[49] G. Blanquart, H. Pitsch, A joint volume-surface-hydrogen multi-variate model for soot formation, in: Combustion generated fine carbonaceous particles, 2009, pp. 437-463.
[50] M. Balthasar, M. Kraft, A stochastic approach to calculate the particle size distribution function of soot particles in laminar premixed flames, Combust. Flame 133 (2003) 289-298.
[51] M. Frenklach, H. Wang, Detailed modeling of soot particle nucleation and growth Int. Symp. Combust. 23 (1991) 1559-1566.
[52] G. Blanquart, H. Pitsch, Analyzing the effects of temperature on soot formation with a joint volume-surface-hydrogen model, Combust. Flame 156 (2009) 1614-1626.
[53] N.A. Fuchs, The Mechanics of Aerosols. Pergamon Press, New York, 1964.
[54] F. Bisetti, G. Blanquart, M.E. Mueller, H. Pitsch, On the formation and early evolution of soot in turbulent nonpremixed flames, Combust. Flame 159 (2012) 317-335.
[55] F. Xu, P. Sunderland, G. Faeth, Soot formation in laminar premixed ethylene/air flames at atmospheric pressure☆, Combust. Flame 108 (1997) 471-493.
[56] J. Appel, H. Bockhorn, M. Wulkow, A detailed numerical study of the evolution of soot particle size distributions in laminar premixed flames, Chemosphere 42 (2001) 635-645.
[57] K. Kuo, R. Acharya, Fundamentals of Turbulent and Multi-Phase Combustion, Wiley, 2012.
[58] A. Eibeck, W. Wagner, Stochastic particle approximations for Smoluchowski's coagulation equation, Annals of Applied Probability, 11(2001) 1137-1165.
[59] A. Kazakov, M. Frenklach, Dynamic Modeling of Soot Particle Coagulation and Aggregation: Implementation With the Method of Moments and Application to High-Pressure Laminar Premixed Flames, Combust. Flame 114 (1998) 484-501.
[60] J. Camacho, C. Liu, C. Gu, H. Lin, Z. Huang, Q. Tang, X. You, C. Saggese, Y. Li , H. Jung, et al., Mobility size and mass of nascent soot particles in a benchmark premixed ethylene flame, Combust. Flame 162 (2015) 3810-3822.
[61] K. Narayanaswamy, G. Blanquart, H. Pitsch, A consistent chemical mechanism for oxidation of substituted aromatic species, Combust. Flame 15 (2010) 1879-1898.
[62] I. Glassman, R.A. Yetter, Combustion (Fourth Edition), Academic Press, 2008, pp. 457-482

Graphical Abstract

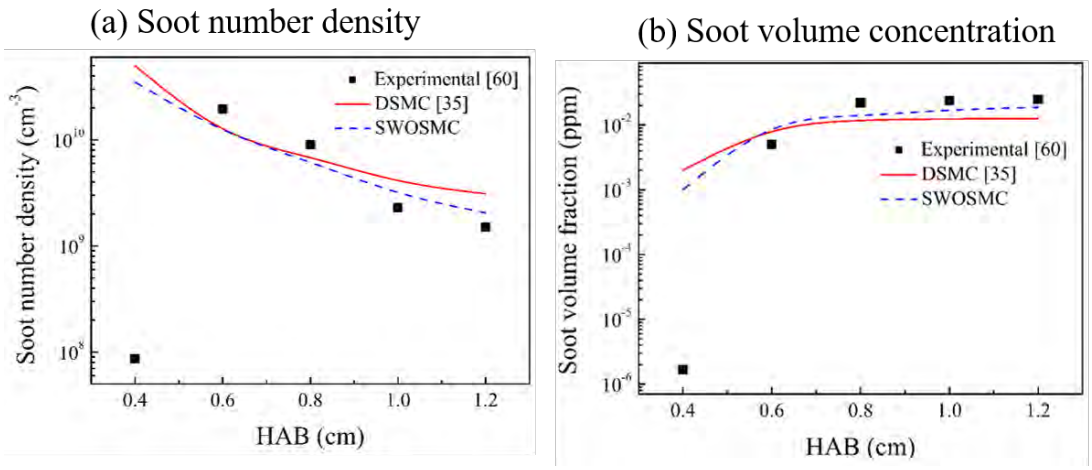

A modified SWOSMC model validation with experimental results [60] and DSMC results [35].

List of Figures

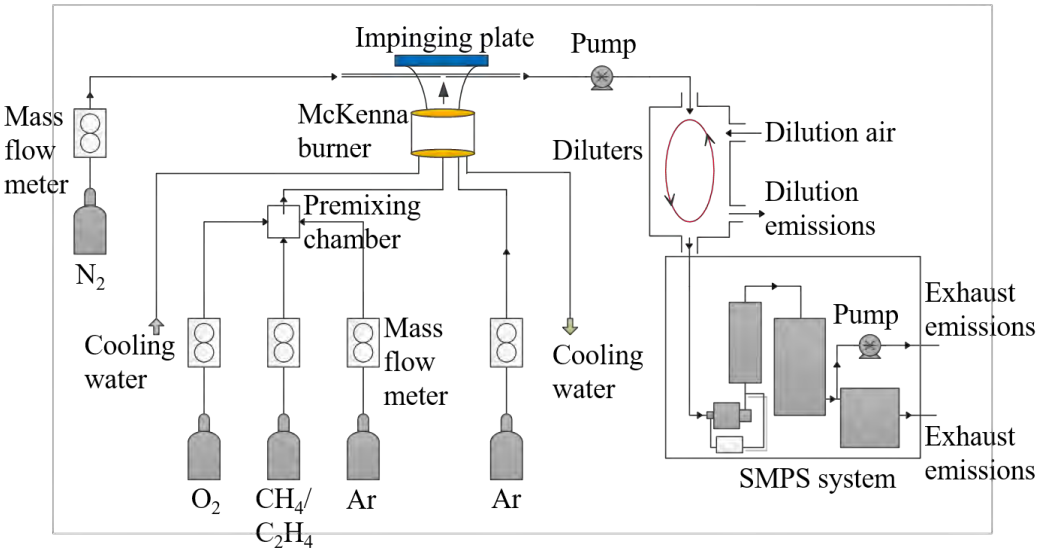

Fig.1. Schematic configuration of experimental apparatus.

(a)

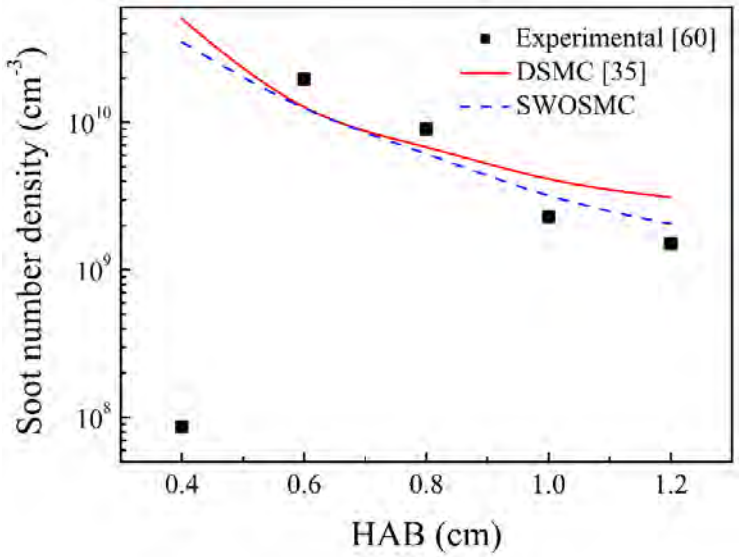

(b)

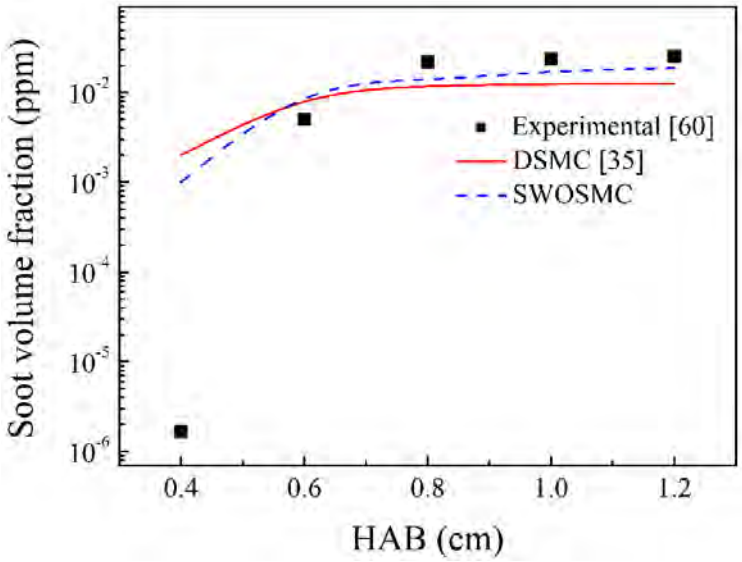

Fig. 2. A modified SWOSMC model validation with experimental results [60] and DSMC results [35]: (a) soot number density and (b) soot volume fraction for different HAB.

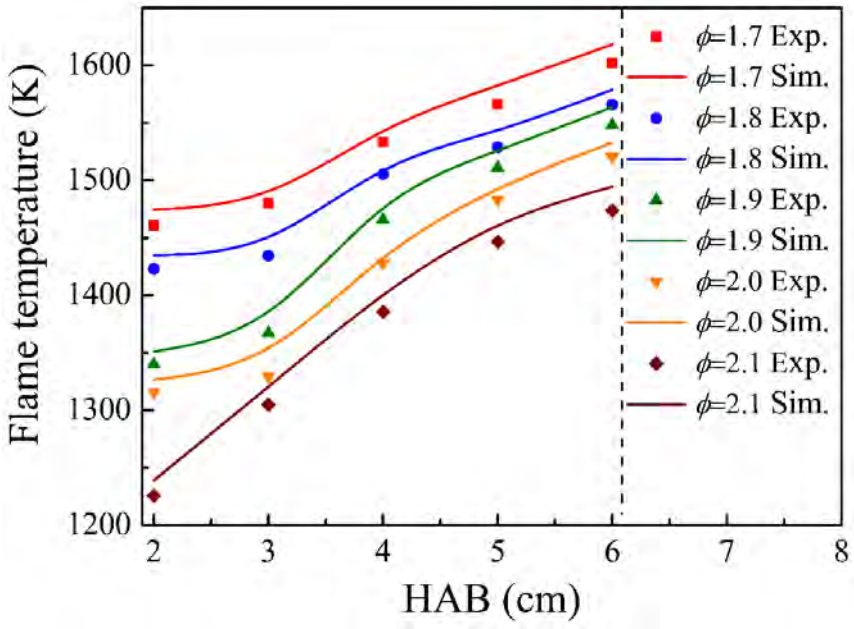

Fig. 3. Flame temperatures of methane at $Re_j = 600$ for different ϕ and HAB.

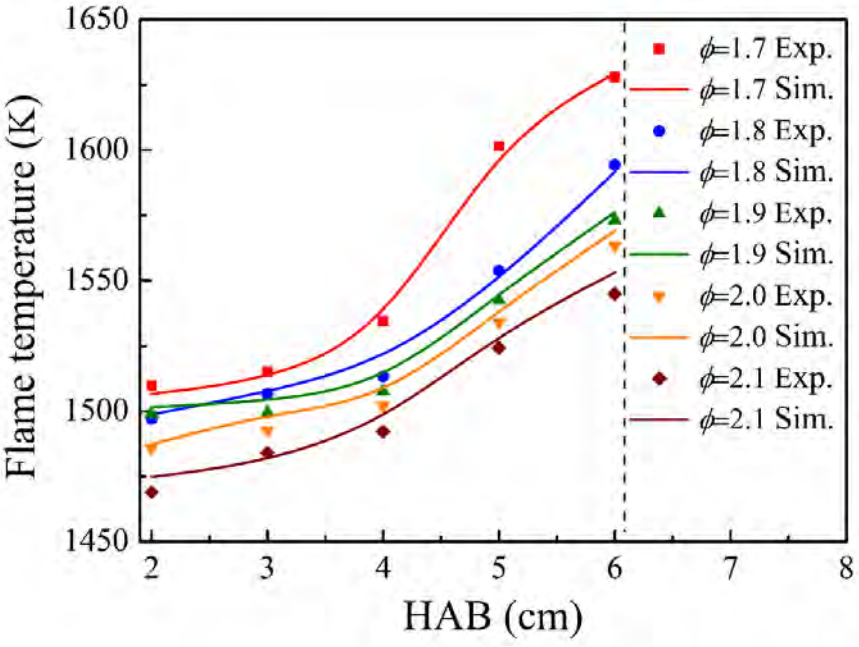

Fig. 4. Flame temperatures of ethylene at $Re_j = 600$ for different ϕ and HAB.

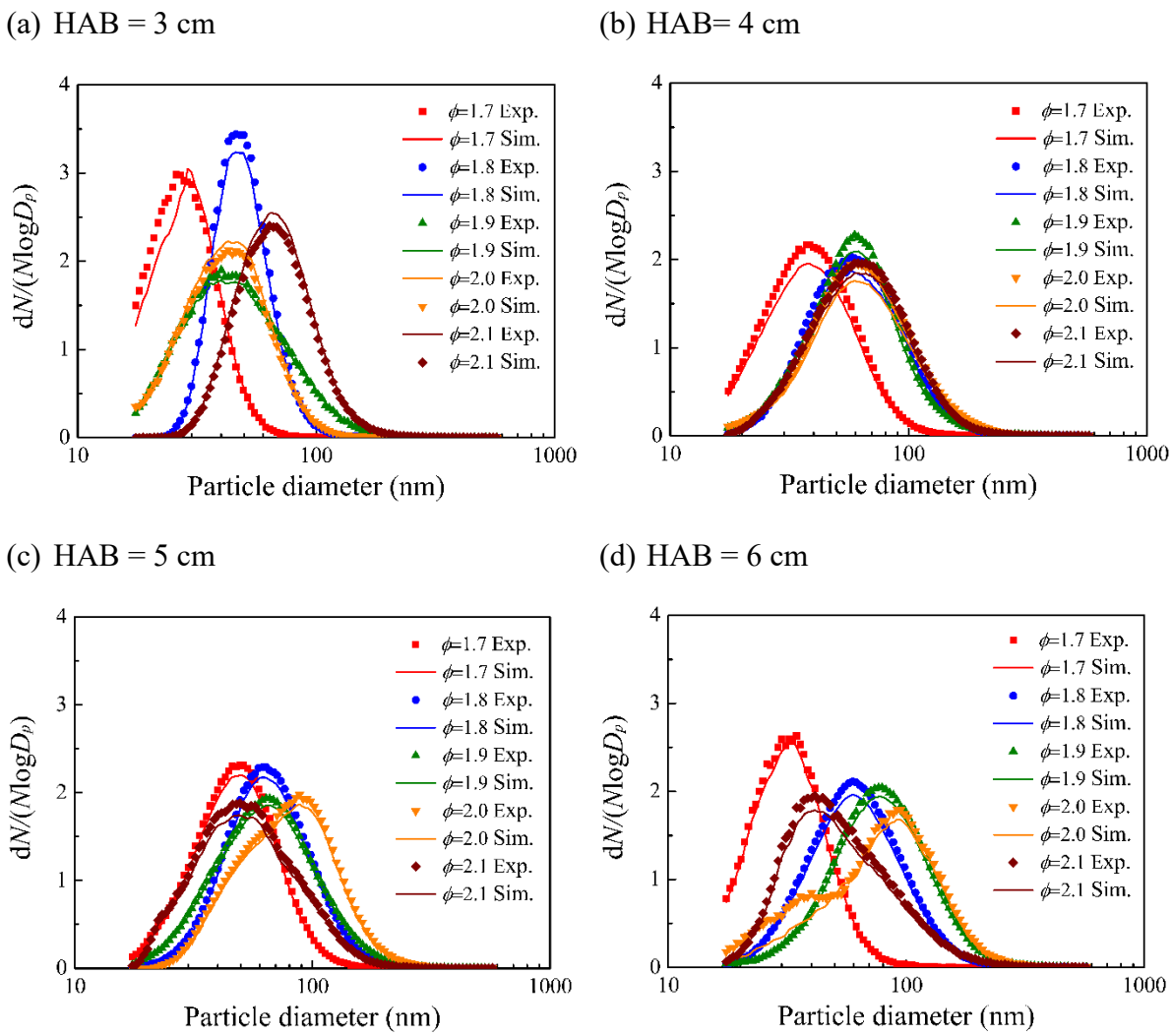

Fig. 5. Soot particle size distribution of methane flame at $Re_j = 600$ for different ϕ and HAB.

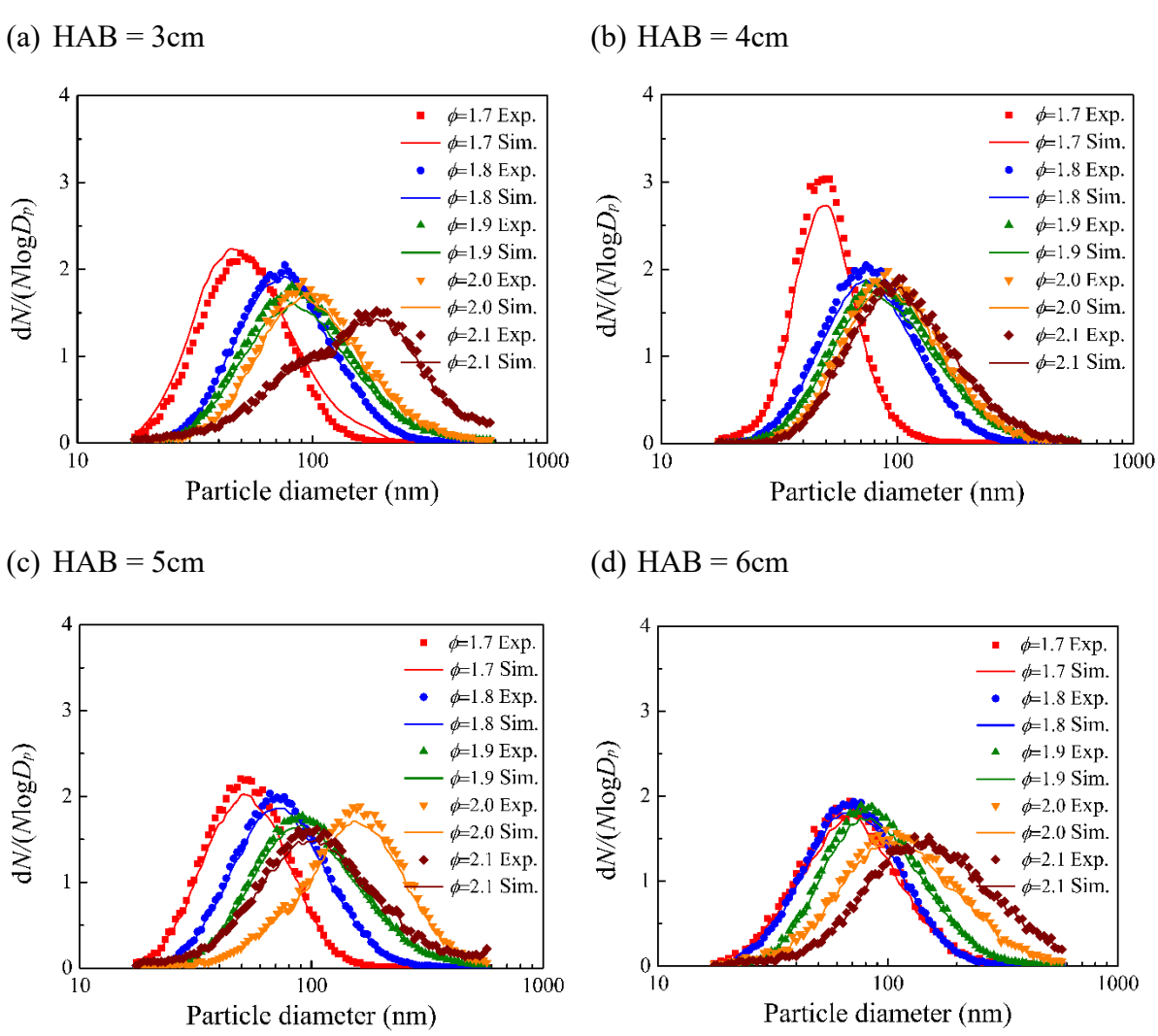

Fig. 6. Soot particle size distribution of ethylene flame at $Re_j = 600$ for different ϕ and HAB.

(a) Normalized total particle number concentration

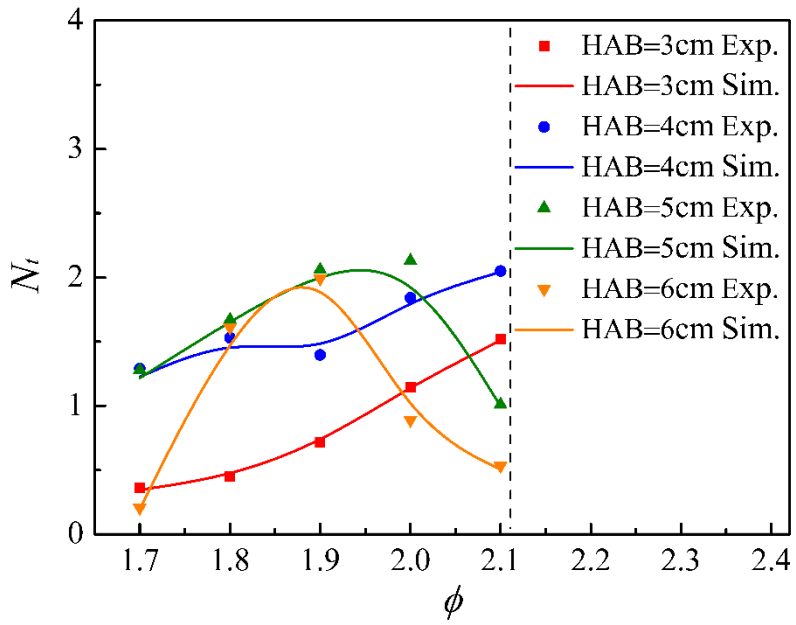

(b) Geometric mean diameter

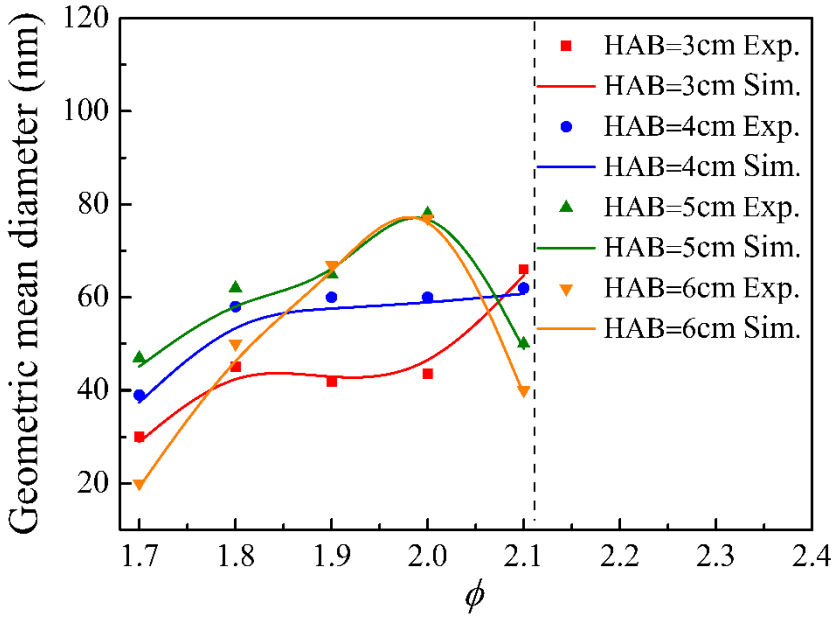

Fig. 7. Normalized total particle number concentration, N_t and geometric mean diameter of soot particles in methane flame at $Re_j = 600$ for different ϕ and HAB.

(a) Normalized total particle number concentration

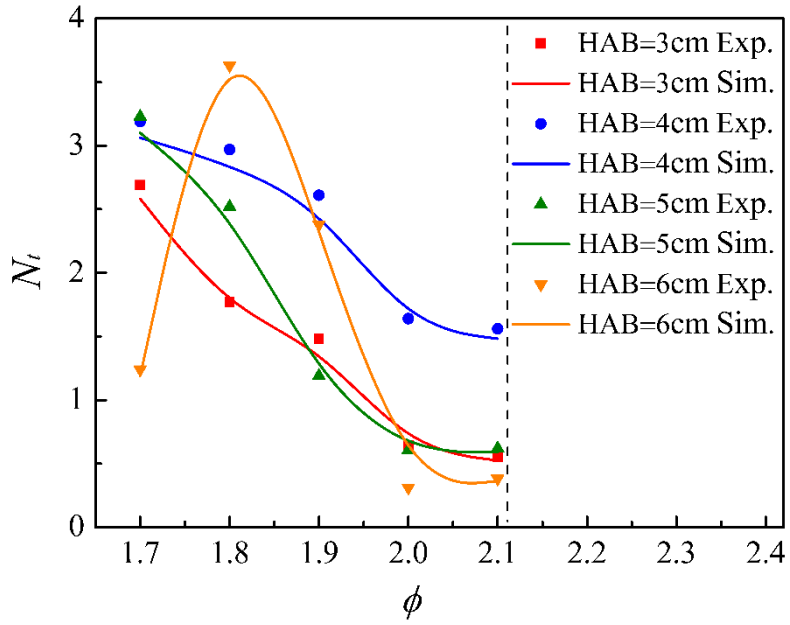

(b) Geometric mean diameter

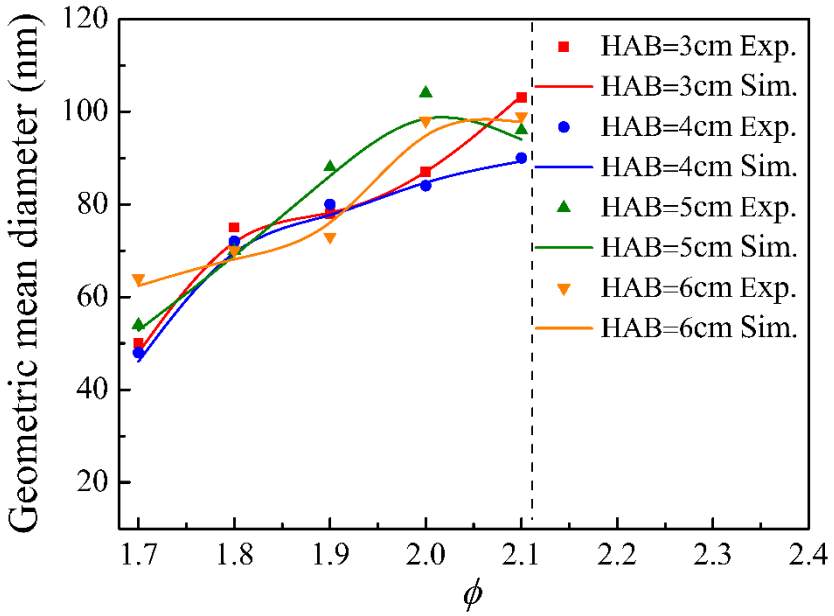

Fig. 8. Normalized total particle number concentration, N_t and geometric mean diameter of soot particles in ethylene flame at $Re_j = 600$ for different ϕ and HAB.

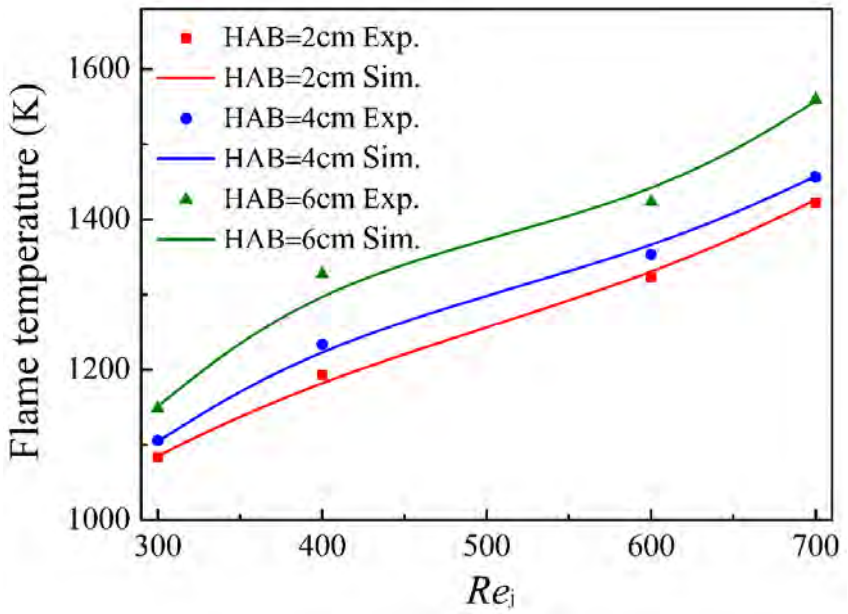

Fig. 9. Flame temperature of methane at ϕ=2.0 for different Re_j and HAB.

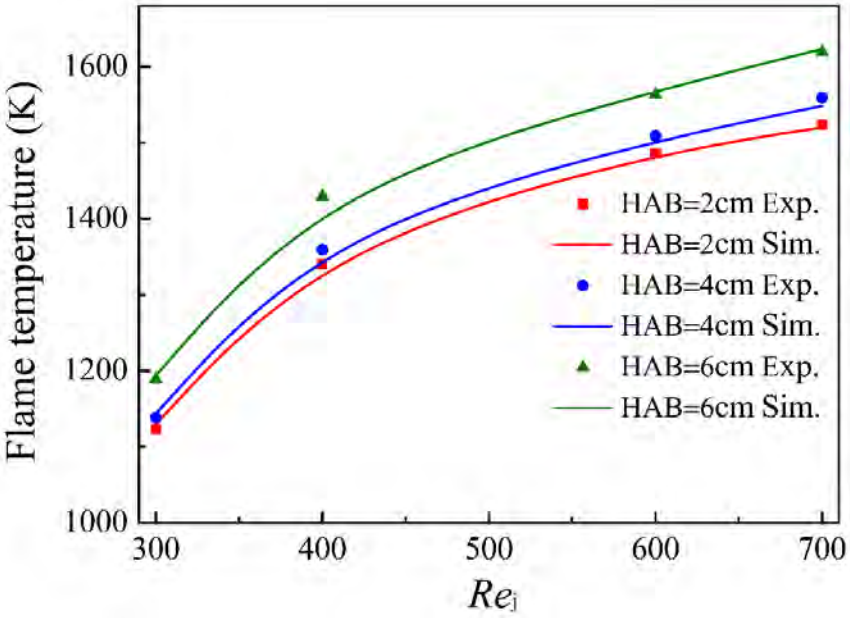

Fig. 10. Flame temperature of ethylene at ϕ = 2.0 for different Re_j and HAB.

(a) HAB = 2cm

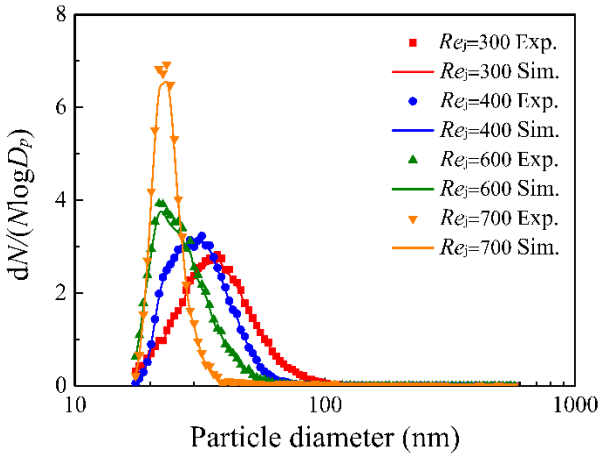

(b) HAB = 4cm

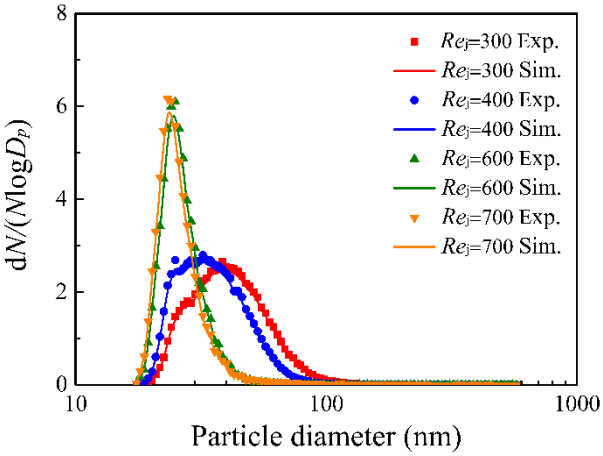

(c) HAB = 6cm

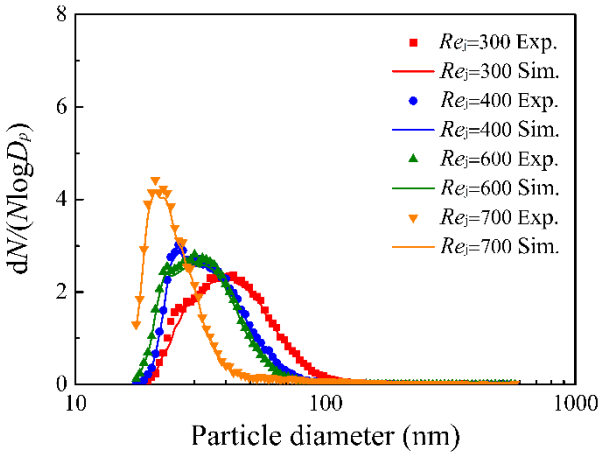

Fig. 11. Soot particle size distribution of methane flame at ϕ=2.0 for different Re_j and HAB.

(a) HAB = 2cm

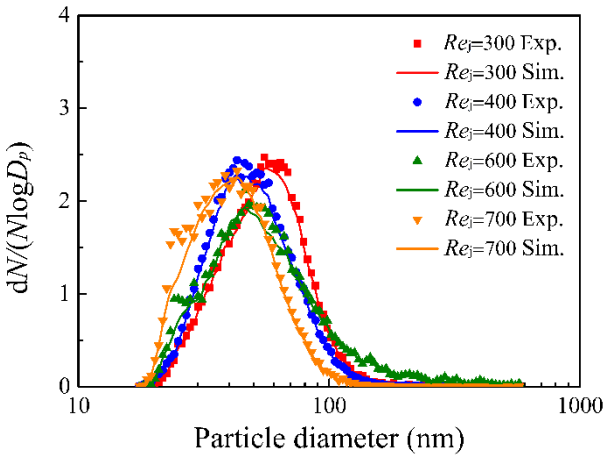

(b) HAB = 4cm

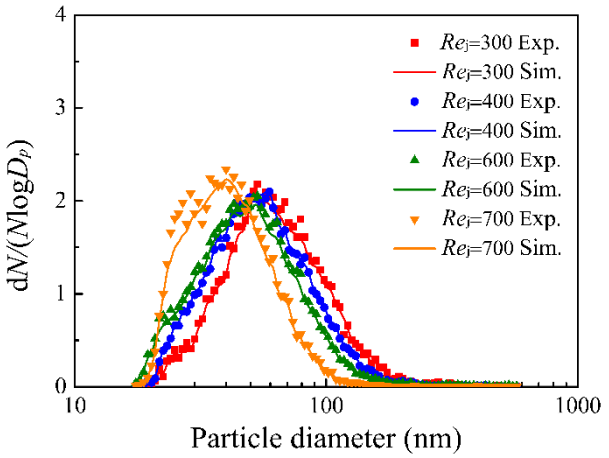

(c) HAB = 6cm

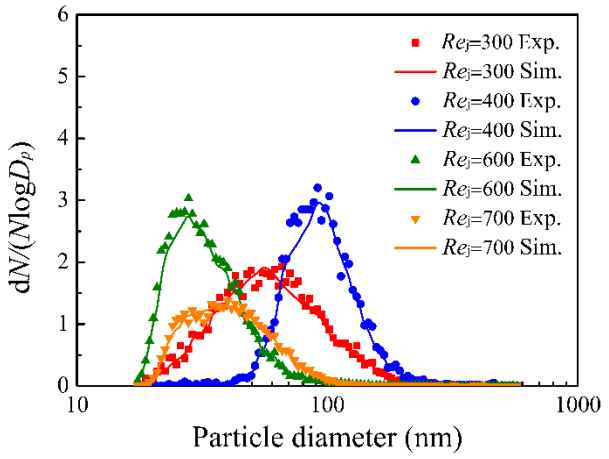

Fig. 12. Soot particle size distribution of ethylene flame at ϕ=2.0 for different Re_j and HAB.

(a) Normalized total number concentration

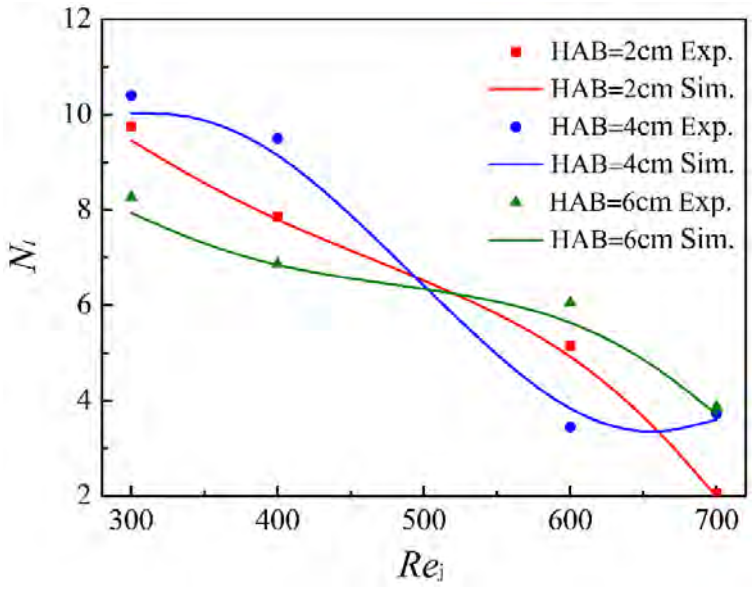

(b) Geometric mean diameter

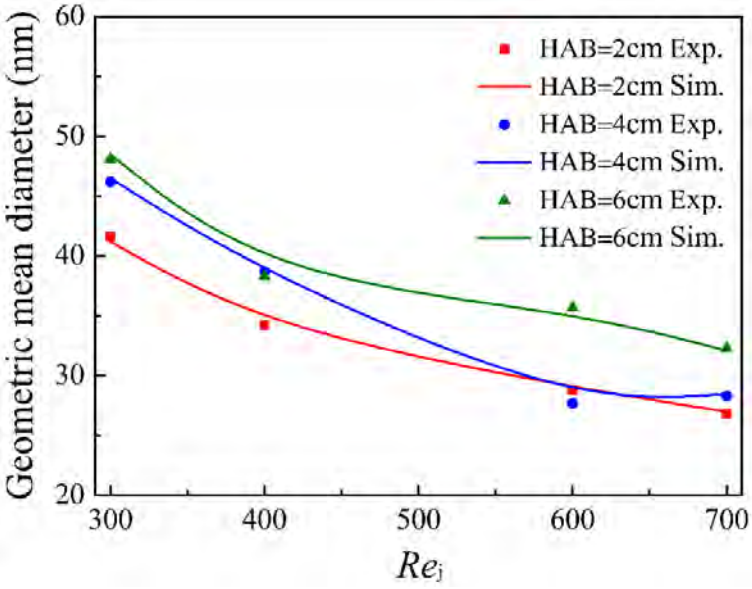

Fig. 13. Normalized total number concentration, N_t and geometric mean diameter of soot particles in methane flame at at $\phi = 2.0$ for different Re_j and HAB.

(a) Normalized total number concentration

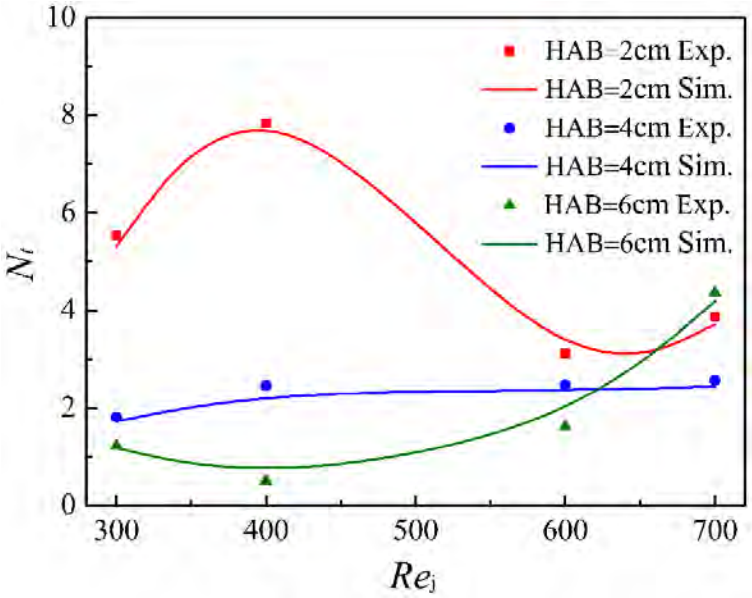

(b) Geometric mean diameter

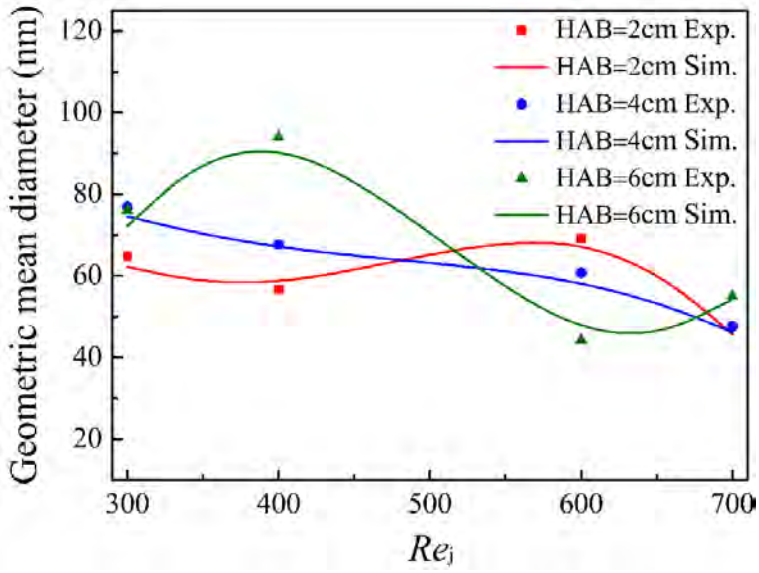

Fig. 14. Normalized total number concentration, N_t and geometric mean diameter of soot particles in ethylene flame at $\phi = 2.0$ for different Re_j and HAB.

List of Table

Table 1 Details of the experimental facility and operation parameters.

Name	Detail
Burner/porous plug	Holthuis flat flame burner (previously referred to as McKenna burner)
Body material	Stainless steel
Plug material	Stainless steel
Plug thickness	1.3 cm
Porosity of the sintered plug	46.5%
Diameter of the burner	6.0 cm
Thermocouple	B type
Fuel gases	Methane (CH_4) and ethylene (C_2H_4)
Oxidant	Oxygen (O_2)
Shielding gas	Argon (Ar)
Equivalence ratio, ϕ	1.7−2.1
Reynolds number of flame jet, Re_j	300−700